

# Upscaling the permeability properties using multiscale X-ray-CT images with digital rock modeling and deep learning techniques

Fei Jiang<sup>1</sup>, Yaotian Guo<sup>1</sup>, Takeshi Tsuji<sup>2</sup>, Yoshitake Kato<sup>3</sup>, Mai Shimokawara<sup>3</sup>, Lionel Esteban<sup>4</sup>, Mojtaba Seyyedi<sup>5</sup>, Marina Pervukhina<sup>6</sup>, Maxim Lebedev<sup>7</sup>, and Ryuta Kitamura<sup>3</sup>

<sup>1</sup>Yamaguchi University

<sup>2</sup>University of Tokyo

<sup>3</sup>JOGMEC

<sup>4</sup>CSIRO-Energy, Oil, Gas & Fuels program

<sup>5</sup>CSIRO

<sup>6</sup>Commonwealth Scientific and Industrial Research Organisation (CSIRO)

<sup>7</sup>Curtin University

November 22, 2022

## Abstract

This study presents a workflow to predict the upscaled absolute permeability of the rock core direct from CT images whose resolution are not sufficient to allow direct pore-scale permeability computation. This workflow exploits the deep learning technique with the data of raw CT images of rocks and their corresponding permeability value obtained by performing flow simulation on high resolution CT images. The permeability map of a much larger region in the rock core is predicted by the trained neural network. Finally, the upscaled permeability of the entire rock core is calculated by the Darcy flow solver, and the results showed a good agreement with the experiment data. This proposed deep-learning based upscaling method allows estimating the permeability of large-scale core samples while preserving the effects of fine-scale pore structure variations due to the local heterogeneity.

1       **Upscaling the permeability properties using multiscale**  
2       **X-ray-CT images with digital rock modeling and deep**  
3       **learning techniques**

4       **Fei Jiang<sup>1,2,3</sup>, Yaotian Guo<sup>1</sup>, Takeshi Tsuji<sup>3,4</sup>, Yoshitake Kato<sup>5</sup>, Mai**  
5       **Shimokawara<sup>5</sup>, Lionel Esteban<sup>6</sup>, Mojtaba Seyyedi<sup>6</sup>, Marina Pervukhina<sup>6</sup>,**  
6       **Maxim Lebedev<sup>7</sup>, Ryuta Kitamura<sup>5</sup>**

7                   <sup>1</sup>Department of Mechanical Engineering, Yamaguchi University, Ube, Japan

8                   <sup>2</sup>Blue energy center for SGE technology (BEST), Yamaguchi University, Ube, Japan

9                   <sup>3</sup>International Institute for Carbon-Neutral Energy Research (WPI-I2CNER), Kyushu University,  
10                   Fukuoka, Japan

11                   <sup>4</sup>Department of Systems Innovation, Faculty of Engineering, the University of Tokyo, Tokyo, Japan

12                   <sup>5</sup>JOGMEC, Chiba, Japan

13                   <sup>6</sup>CSIRO Energy BU, Perth, Australia

14                   <sup>7</sup>Curtin University, Perth, Australia

15       **Key Points:**

- 16       • A workflow is proposed to estimate the upscaled absolute permeability of the rock  
17       core direct from CT images.
- 18       • A deep learning technique is adopted to establish correlations between high-resolution  
19       computed permeability and low-resolution images.
- 20       • The upscaling method allows estimating the large-scale permeability while pre-  
21       serving the effects of fine-scale permeability variations.

---

Corresponding author: Fei Jiang, [fjiang@yamaguchi-u.ac.jp](mailto:fjiang@yamaguchi-u.ac.jp)

## Abstract

This study presents a workflow to predict the upscaled absolute permeability of the rock core direct from CT images whose resolution are not sufficient to allow direct pore-scale permeability computation. This workflow exploits the deep learning technique with the data of raw CT images of rocks and their corresponding permeability value obtained by performing flow simulation on high resolution CT images. The permeability map of a much larger region in the rock core is predicted by the trained neural network. Finally, the upscaled permeability of the entire rock core is calculated by the Darcy flow solver, and the results showed a good agreement with the experiment data. This proposed deep-learning based upscaling method allows estimating the permeability of large-scale core samples while preserving the effects of fine-scale pore structure variations due to the local heterogeneity.

## 1 Introduction

The flow behavior in porous rocks plays a vital role in many scientific and engineering fields, such as oil and gas recovery (Lake et al., 2014), geothermal energy (Tester et al., 2006), and geologic carbon storage (Juanes et al., 2006). The permeability property is the most important parameter to characterize the fluid transport in porous media, which strongly depends on the pore structure. The heterogeneity of pore structure usually varies significantly across a wide range of length scales, which leads to scale dependence of permeability (Worthington, 2004). The issue of scale and heterogeneity make the prediction of permeability extremely difficult.

With the availability of three-dimensional imaging techniques, we are able to investigate the detailed structural heterogeneity of rocks at different scales: at the nano ( $nm$ ) scale using nano-CT imaging (Goral et al., 2019), at the pore ( $\mu m$ ) scale using micro-CT imaging (Blunt et al., 2013), and at the core ( $cm$ ) scale using medical-CT imaging (Zhai et al., 2020). However, very few studies have been conducted on establishing linkage among these scales (Dehghan Khalili et al., 2013; Menke et al., 2021), and the scaling behavior of permeability is difficult to predict. Khalili et al. (2013) focus on carbonate reservoir rock and investigate the use of porosity-permeability relationships derived from micro-CT images to estimate permeability on a larger scale by the renormalization technique. More recently, Menke et al. (2021) applied the multivariate regression method to upscale and predict permeability from the pore scale to the Darcy-scale by deriving an upscaled porosity-permeability relationship. However, no studies have yet estimated the upscaled permeability directly from the large-scale raw CT images with low resolution. The lower resolution CT images provide greater sample coverage, therefore it is able to capture more sample heterogeneity, but do not adequately represent the correct pore structure, which is essential for computing the permeability using the direct simulation method (Botha & Sheppard, 2016). Previous studies (Fredrich et al., 1993; Pape et al., 1999) have proven that absolute and relative permeability are strongly dependent on pore space geometry. Therefore, accurate flow and other physical properties can only be obtained by carrying out physical simulations on high-resolution CT images that accurately represent the pore geometries and characterize all major flow paths in the rock. Arns et al. (2001) investigated the effects of image resolution on the computation of electrical conductivity. They observed that low image resolution causes the over-estimation of the formation factor. On the other hand, the high-resolution CT images are able to resolve well the pore structure permitting direct simulation of fluid flow and accurately estimate the permeability property (Jiang & Tsuji, 2017; Blunt et al., 2013; Shah et al., 2016). Direct simulations like Lattice Boltzmann Methods (LBM) or Finite Volume Methods (FVM) to solve the Navier Stokes Equation (NSE) can be performed at the pore spaces of rocks extracted from the high-resolution CT images (Raeini et al., 2012; Jiang & Tsuji, 2014, 2015, 2017). However, the direct simulation requires a large amount of computational resources and is time consuming. In addition, high resolution leads to a smaller

74 field of view and can only cover a small representative volume for the very homogeneous  
75 rocks. For rock samples exhibiting heterogeneity above the field of view, a low-resolution  
76 CT image with large sample coverage is required. However, the low-resolution images  
77 cannot provide enough accuracy for the computation of physical properties. Therefore,  
78 integration of the physical informations obtained from high-resolution CT images at a  
79 small scale into the low-resolution CT image data at a large scale is an efficient way to  
80 improve the prediction accuracy of the permeability. To systematically propagate the  
81 effects of small-scale geological variations observed in high-resolution CT images up to  
82 the large core-scale low-resolution CT images, we need an upscaling method. The up-  
83 scaling requires developing a reliable equivalent model on a coarser scale, which can rep-  
84 resent the behavior of fine-scale model in an averaged sense. The homogenization the-  
85 ory is a widely used upscaling technique that can compute an effective property for pe-  
86 riodic structures (Z.-J. Xu, 2012). However, it is doubtful whether such a mathemati-  
87 cal homogenization process can be used to model the permeability of natural rocks be-  
88 cause they are rarely periodic. A reliable upscaling process requires analyzing the wealth  
89 of imaging data in order to characterize the inherent rock heterogeneities at multiple scales  
90 (Menke et al., 2021).

91 Recently, the deep learning technology holds a solid potential to extract the char-  
92 acteristics of pore geometry from the CT images (Bizhani et al., 2022). The features of  
93 rock CT images have been investigated using various neural networks (Da Wang et al.,  
94 2019) with many extended applications (Wang, Blunt, et al., 2021). For instance, the  
95 synthetic rock image reconstruction has been successfully performed by using the Gen-  
96 erative Adversarial Networks (GAN), which reproduces the similar characteristics of nat-  
97 ural rocks (You et al., 2021). In addition, the 3D image-based digital rock physical mod-  
98 elling can also be enhanced with deep learning techniques to predict petrophysical prop-  
99 erties such as permeability (Suzuki et al., 2022), relative permeability and the distribu-  
100 tion of fluid phases (Wang, Blunt, et al., 2021). Santos et al. (2020) used a convolutional  
101 neural network (CNN) to predict the flow velocity fields inside the pore spaces directly.  
102 Rabbani and Babaei (Rabbani & Babaei, 2019) successfully estimated the permeabil-  
103 ity of the pore-network model from the geometric properties using a regression method  
104 based on an Artificial Neural Network (ANN). Alqahtani et al.(2021) predicted the per-  
105 meability directly from the CT images by 3D CNN regression. However, very few stud-  
106 ies have been conducted on applying of deep learning techniques to upscale permeabil-  
107 ity. This study aims to combine the deep learning technique and digital rock physics to  
108 predict the permeability of large-scale core with the information from the small-scale mi-  
109 cro samples. The 3D CNN based deep learning techniques are used to establish corre-  
110 lations between low-resolution image characteristics and high-resolution computed per-  
111 meability by overlapping registered CT images derived at different resolutions spanning  
112 orders of magnitude in length scales. The CNN networks are trained using the dataset  
113 of directly calculated permeability values based on high-resolution CT images and the  
114 corresponding low-resolution raw images. Then, a workflow is proposed to predict and  
115 map the absolute permeability variations over the large fields of view from the low-resolution  
116 images by the trained CNN networks. Finally, the upscaled permeability is calculated  
117 by inputting the predicted permeability map at the whole core scale into a Darcy flow  
118 solver. Our proposed upscaling approach benefits from both the large field of view by  
119 the low-resolution CT and the high accuracy of flow property computation by the high-  
120 resolution CT.

## 121 2 Rock samples

122 A Boise sandstone core was used in this study as it offers a range of pore size, grain  
123 size, mineralogy, and geological structures that are not too complex for modelling pur-  
124 poses of permeability upscaling. Boise is sandstone with 40% quartz and about 50% feldspars  
125 with a brine porosity and permeability at about 24% and 2.8D, respectively. The pore

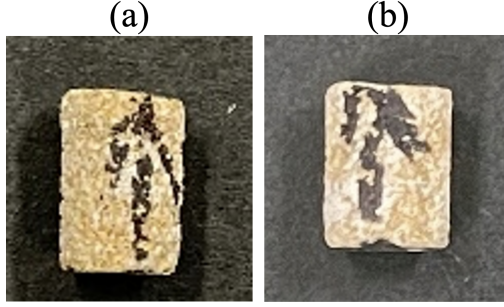


**Figure 1.** Boise sandstone: (a) sample I (b) sample II.

126 size distribution is around  $50 \mu m$ , and the grain size distribution is around  $100 \mu m$ , which  
 127 are measured from thin section optical images. Here, we extracted two small core sam-  
 128 ples (samples I and II) with a diameter of 6.8mm out of the whole meter scale rock sam-  
 129 ple (Fig. 1). These two small samples have lengths of about 1.0 cm. Micro X-ray CT  
 130 imaging for these samples was conducted using the micro CT scanner (Xradia Versa XRM-  
 131 500) with two resolutions:  $2\mu m/\text{voxel}$  (fine) and  $8\mu m/\text{voxel}$  (coarse).

### 132 3 Method

133 The permeability upscaling method mainly contains three parts: (1) build a neu-  
 134 ral network trained by the datasets consisting of pairs of the sub-volumes from the coarse  
 135 scanned 3D CT images (low resolution) and their corresponding permeability value ob-  
 136 tained by the direct flow simulation on fine scanned CT images (high resolution) (2) pre-  
 137 dict the permeability distributions directly from the coarse scanned 3D CT images of  
 138 the whole core using the neural network; (3) calculate the upscaled permeability by Darcy-  
 139 scale flow simulations using the predicted permeability map.

140 For the first part, we propose a workflow aimed at predicting absolute permeabil-  
 141 ity direct from low-resolution images using a deep learning technique combined with di-  
 142 rect flow simulation on high-resolution images. Calculating permeability directly based  
 143 on the low-resolution CT is difficult because the low resolution usually causes connect-  
 144 ing narrow pore throats to be represented by blurred grayscale values and leads to the  
 145 limitation of obtaining the accurate pore structure in pore scale. Due to the inability of  
 146 resolving high-quality pore structures, low resolution CT images are inadequate for di-  
 147 rect flow simulation. Therefore, the accurate permeability data must be evaluated based  
 148 on the high-resolution CT images. However, high-resolution usually leads to a small fields  
 149 of view, which is inadequate for heterogeneous porous media. On the other hand, low-  
 150 resolution micro CT images give larger sample coverage and are therefore more repre-  
 151 sentative of heterogeneous systems on a large scale. Our proposed workflow involves com-  
 152 puting permeability from high-resolution micro-CT images and registration of the cor-  
 153 responding low-resolution images on a large scale. This approach benefits from the ac-  
 154 curate permeability data obtained from well-resolved pore structure at a small scale and  
 155 large field of view characterizing the spatial heterogeneity. Deep learning regression tech-  
 156 niques are used for predicting and mapping permeability variations in larger-scale low-  
 157 resolution images. Binarization of the low-resolution images is unnecessary since the raw  
 158 images data can be directly input into the deep learning neural network using CNN. Once  
 159 the neural network is trained with the dataset of directly calculated permeability val-  
 160 ues and corresponding low-resolution raw images, we are able to predict the permeabil-  
 161 ity map over the whole domain of the large sample. Finally, the upscaled permeability

of the entire rock core can be calculated by the Darcy flow solver based on the permeability map. The detailed workflow contains the following steps (Fig. 2):

1. Micro-CT coarse scanning of the whole core (1.0 cm in length) with low resolution ( $8\mu\text{m}/\text{voxel}$ ) (left-hand side image in Fig. 2 (a));
2. Selection of location for close-up view region (2 mm wide) and micro-CT fine scanning with high resolution at the pore-scale ( $2\mu\text{m}/\text{voxel}$ ) (right-hand side background image in Fig. 2 (a));
3. Noise reducing and segmentation of the fine scanned micro-CT images (black-white area of the right-hand side image in Fig. 2 (a));
4. Extracting of sub-volumes (grids in Fig. 2 (a) right) from the segmented images with high resolution ;
5. Calculation of permeability properties from the extracted high-resolution sub-volumes using LBM;
6. Identifying the same area of sub-volumes on the coarse scanned images of the whole core (registration of the overlap region at different resolutions) (Fig. 2 (a));
7. Linking the permeability data to the corresponding low-resolution area in coarse scanned 3D CT images and create the training datasets consisting of pairs of low-resolution 3D images and their corresponding permeability value;
8. Training the neural network with the prepared datasets (Fig. 2 (b));
9. Predicting the permeability map of the whole core by the trained neural network (Fig. 2 (c));
10. Calculating the flow flux inside the whole core by Darcy flow solver (Fig. 2 (d)); and
11. Estimate the upscaled permeability of the whole rock core area.

In this method, the CNN regression model establishes a relationship between low-resolution images and high-resolution computed permeability. In such a way, the highly accurate information obtained from small-scale high-resolution images can be upscaled to a large domain. This approach has great potential to enable the upscaling of any physical properties from small pore scales to large core scales.

### 3.1 Training dataset acquisition

The whole sample was first imaged by the micro-CT scanner with low resolution ( $8\mu\text{m}$ ) to cover the entire core area (Fig .3). Then the center area of the sample was selected as ROI (region of interest) and scanned with fine resolution ( $2\mu\text{m}$ ). The fine resolution was determined to capture the pore structure well enough for calculating the permeability of the extracted sub-volumes using pore-scale flow simulation. To improve the image quality, a non-local means filter was applied to the fine CT images. The filter cancels most of the salt-n-pepper noise, making the image smoother and more uniform while preserving boundaries. Afterwards, the datasets of high-resolution underwent a segmentation routine for extracting the binary pore geometry. The segmentation is based on a simple threshold (histogram-based) algorithm which assigns labels to voxels according to their intensities. The threshold values were chosen based on the local minimum values of the histograms of the image intensities. Note that only high-resolution images need to be processed and segmented for direct flow simulation. In contrast, the original raw images with low resolution can be directly used for deep learning. Finally, a binarized pore-geometry model with voxels of  $690\times 690\times 5000$  was cropped from the cylindrical sample area and reconstructed (Fig .3). Then the binarized model was divided into small  $200^3$  sub-volumes (dark red cubes in Fig .3). This size of sub-volume is smaller than the size of the representative volume element (RVE), which is recommended for deep learning in order to increase the variety of sub-volumes in terms of porosity and permeability (Hong & Liu, 2020). To meet the the demand of large datasets, the sub-volumes are allowed to be overlapped with 100 voxels during the extraction (red grids in Fig .3). The

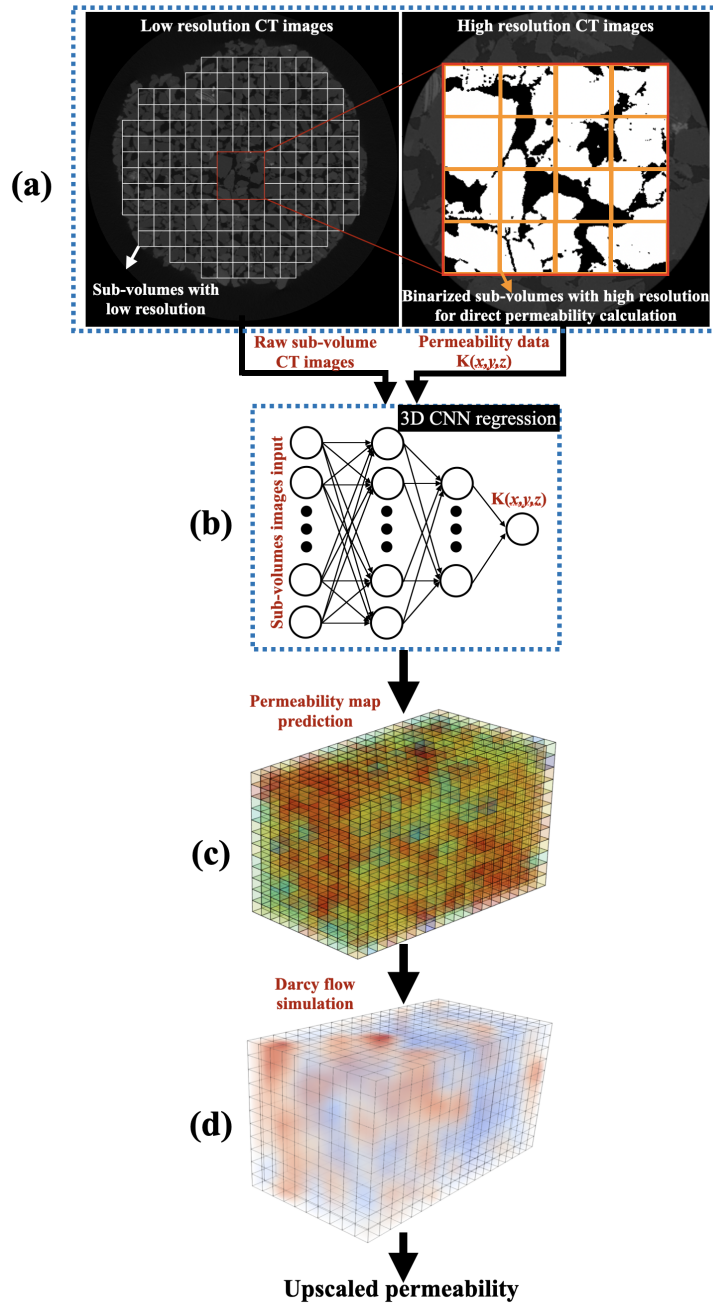


**Figure 2.** Permeability upscaling workflow: (a) micro-CT scanning and preparation of the training dataset; (b) neural network training with the prepared CT images and permeability data; (c) predicted permeability map of the whole core by the trained neural network; (d) flow flux distribution inside the whole core calculated by the Darcy flow solver.

213 permeability of these sub-volumes was calculated by the LBM flow solver described in  
 214 Section 3.3. The corresponding sub-volumes with low-resolution at the same location in  
 215 the sample were then extracted directly from the original coarse-scanned images (grayscale  
 216 cubes in Fig. 3). Since the fine-scanned and coarse-scanned images have four times ( $4\times$ )  
 217 resolution difference, the dimension of the low-resolution sub-volume is  $50 \times 50 \times 50$ .  
 218 In this way, we obtained the dataset for deep learning consisting of pairs of a low-resolution  
 219 sub-volume and its permeability value (black box in Fig. 3). The total number of the  
 220 sub-volumes is 8000 for each sample. In our study, 90% of the data are used as the train-  
 221 ing data while the rest 10% data are used for testing data.

### 222 3.2 Registration of images at different scales

223 For a single rock core sample, since the coarse scan with low resolution is conducted  
 224 along with the fine scan with high resolution at different scales, we have to identify the  
 225 same area at both resolutions. Therefore, the position of the sample was carefully set  
 226 to keep the same scanning angle during the two scans for the convenience of image reg-  
 227 istration. Correlating the fine scanned data to coarse scanned data can be easily con-  
 228 ducted with the reference CT slice of the same depth from the top of the core sample.  
 229 An example of image registration across two length scales is shown in Fig. 4, where the  
 230 matching area with high resolution is shown for the same region in the low-resolution  
 231 whole core images. In such a way, direct observation of the same property for the same  
 232 domain at different resolutions becomes possible. The accurate registration of the center  
 233 core into the whole core allows the information learned at a higher resolution but on  
 234 a smaller volume to be upscaled into the whole. The corresponding sub-volume at low  
 235 resolution is carefully searched in the whole core images to match the binarized high-  
 236 resolution sub-volume.

### 237 3.3 Direct simulation for the acquisition of ground truth flow data

238 Recently, direct pore-scale simulation has been widely used to obtain flow prop-  
 239 erties from digital rock CT images (Boek & Venturoli, 2010; J. Yang & Boek, 2013; Jiang  
 240 & Tsuji, 2017; L. Yang et al., 2019). In this study, we adopt the LBM to calculate the  
 241 flow field in the complex pore spaces. The LBM is an efficient and accurate method for  
 242 both single-phase and multiphase flow simulation (Liu et al., 2021; Li et al., 2021; Jiang  
 243 et al., 2021; Zhang et al., 2022; Jiang et al., 2022) directly on the raw images of rocks.  
 244 The LBM can approximately recover Navier Stokes equations from kinetic theory (Shan  
 245 et al., 2006). In LBM, particle distribution functions (PDF)  $f_i(\mathbf{x}, t)$  are introduced to  
 246 represent the probability of encountering a fluid pseudo-particle with velocity  $\mathbf{e}_i$  and spa-  
 247 tial position  $\mathbf{x}$  at time  $t$ .

$$f_i(\mathbf{x} + \mathbf{e}_i \delta t, t + \delta t) = f_i(\mathbf{x}, t) + \Omega_i(\mathbf{x}, t) \quad (1)$$

248 where  $\mathbf{e}_i$  is the lattice velocity in the  $i$ th direction,  $\delta t$  is the time step, and  $\Omega_i$  is the col-  
 249 lision operator. A three-dimensional lattice with 19 velocity vectors (D3Q19) is used in  
 250 the present study (Guo & Shu, 2013). To improve the numerical stability and remove  
 251 the uncertainty due to viscosity-dependence (Pan et al., 2006), the multiple-relaxation-  
 252 time (MRT) collision operator (d’Humières, 1992) is adopted.

253 Single-phase flow is simulated until the steady-state conditions are achieved. The  
 254 steady state is determined by tracking the change of average velocity in pore spaces. When  
 255 the relative change in average velocity is less than  $10^{-5}$ , the simulation is considered to  
 256 converge. The permeability can be calculated by

$$K = \frac{\mu \bar{v} L}{\Delta P} \quad (2)$$

257 where,  $\bar{v}$  is the mean velocity in the flow direction,  $\mu$  is the kinematic viscosity of the fluid,  
 258  $L$  is the length of the domain along the flow direction, and  $\Delta P$  is the pressure difference

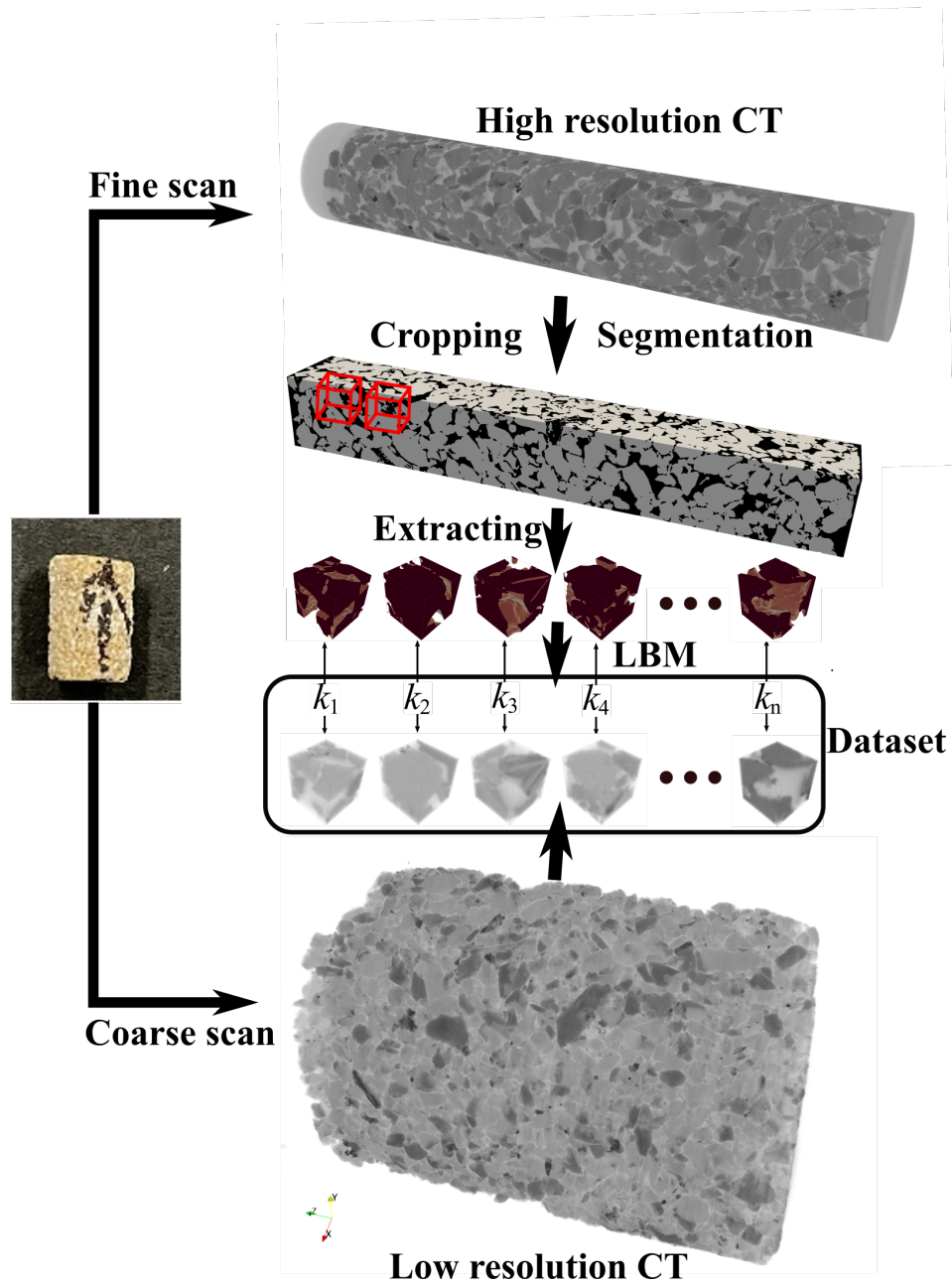


**Figure 3.** Workflow of training dataset acquisition. The dataset consists pairs of low resolution sub-volumes and its permeability value calculated by LBM solver based on the corresponding high resolution sub-volumes.

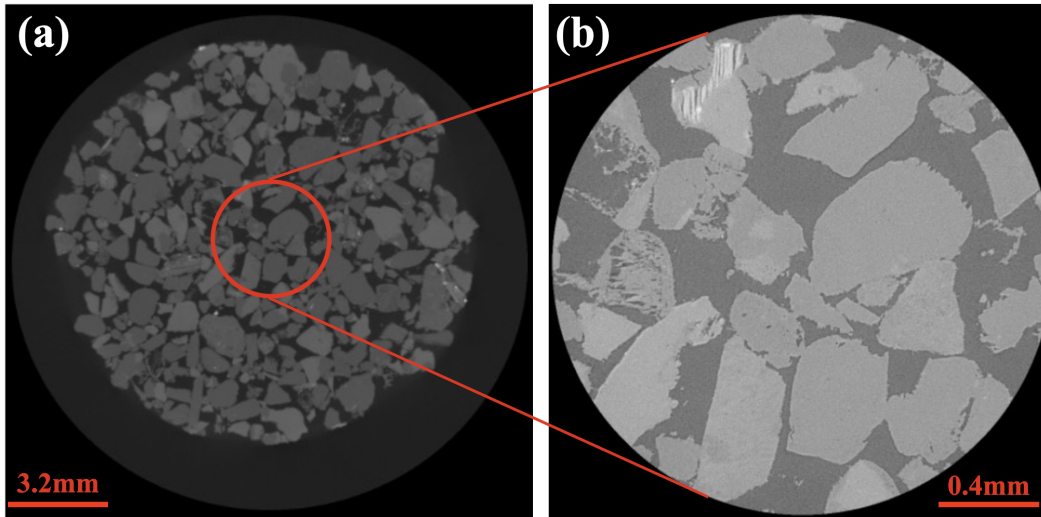


**Figure 4.** Registration of micro-CT images with two different resolutions: (a) low resolution CT for whole rock core (b) high resolution CT for center core region.

259 between the inlet and outlet. In our simulation, a constant pressure drop between in-  
 260 let and outlet is applied by using a body force mimicking the local pressure gradient, and  
 261 the no-slip wall boundary conditions are imposed on the grain surfaces. The pressure  
 262 gradient is set sufficiently low to ensure the Reynolds number small enough to reproduce  
 263 Stokes-regime flow. We applied a periodic condition at all outer boundaries of the core  
 264 cube. Specifically, for the flow direction, the sample was mirrored to ensure that the pore  
 265 spaces on the right side were connected to the left side.

### 266 3.4 Convolutional neural networks for predicting permeability

267 The convolutional neural network (ConvNets) (LeCun et al., 1998) is the basis of  
 268 typical deep learning models, which consist of a sequence of nonlinear transformations  
 269 implemented as convolutional layers (N. J. Alqahtani et al., 2021). In this study, six net-  
 270 work architectures of ConvNets: Conv8, VGG16, VGG19 (Simonyan & Zisserman, 2014),  
 271 GoogLeNet-V1, GoogLeNet-V3 (Szegedy et al., 2015), ResNet34 (He et al., 2016) are  
 272 adopted for permeability prediction. The details of those network architectures are pre-  
 273 sented in Appendix A. The most simple Conv8 network consists of four convolution blocks,  
 274 including a 3D convolutional layer, batch normalization (Ioffe & Szegedy, 2015), and a  
 275 rectified linear unit (ReLU) as a activation function (Nair & Hinton, 2010), followed by  
 276 a Global Average Pooling layer (GAP) and four dense layers (Fig. A1). The final con-  
 277 volutional layer was vectorized by the GAP layer and then fed into fully connected dense  
 278 layers. The function of the GAP layer is to bridge the convolutional structure with tradi-  
 279 tional neural networks. The 3D CNN enables obtaining the feature map containing vol-  
 280 umetric contextual information in all three dimensions. In this study, the Conv8 is the  
 281 most shallow network for performance comparison.

282 VGG (Simonyan & Zisserman, 2014) is a deeper version of the ConvNet architec-  
 283 ture (Fig. A2 and A3). In VGG, only the  $3 \times 3 \times 3$  size of the convolution layer filter is  
 284 used. Such a small-scale convolution filter helps accelerate the learning process. The ac-  
 285 tivation function with ReLU is always added after the convolution layer. VGG16 is a net-  
 286 work of 16 layers deep and consists of five max-pooling layers in each convolution block.  
 287 Three dense layers are applied before the output layer. The architecture of VGG19 is

288 similar to the VGG16, except the network is 19 layers deep (3 more convolutional lay-  
 289 ers).

290 GoogLeNet (Szegedy et al., 2015) introduced the concept of the inception module  
 291 (network-in-network), which is built by a combination of small-scale convolution layers  
 292 (Fig. A4 and A5). In this inception module, multiple convolution layers with different  
 293 sizes ( $1\times 1$ ,  $3\times 3$ ,  $5\times 5$ ) are applied in parallel and the outputs of each convolution layer  
 294 are then concatenated. Usually, to realize a deeper and more expressive network, the num-  
 295 ber of weights significantly increases, resulting in a longer training time. By the intro-  
 296 duction of a module consisting of a bunch of small convolution filters, GoogLeNet achieves  
 297 a good trade-off between model performance and the number of weights, and the amount  
 298 of computation cost can be greatly reduced. The improved V3 version of GoogLeNet de-  
 299 composes  $3\times 3$  convolutions into two one-dimensional convolutions ( $1\times 3$ ,  $3\times 1$ ), which  
 300 can both improve the calculation speed and increase the depth and nonlinearity of the  
 301 network. In the original GoogLeNet, the auxiliary loss units are added to branch off from  
 302 the middle of the network. The auxiliary loss unit can prevent gradient vanishing for clas-  
 303 sification problems by propagating the error directly to the middle layer of the network.  
 304 In our regression problem, we modified the network by replacing the last 3 layers with  
 305 a fully connected dense layer and a regression layer and removing the auxiliary loss unit.

306 The deeper layers caused the gradient loss problem and the degradation problem,  
 307 making learning more difficult. ResNet (He et al., 2016) solves the gradient vanishing  
 308 problem by introducing a mechanism called shortcut connection, which directly adds the  
 309 inputs of the front layer to the back layer. The basic ResNet block contains two convo-  
 310 lutional layers each, followed by batch normalization and a ReLU. The shortcut connec-  
 311 tion links the top of the basic block to just before the ReLU after the second convolu-  
 312 tional layer in the block. This shortcut connection is able to skip the nonsucceeding lay-  
 313 ers for the very deep model.

314 In this study, all the networks are implemented using the TensorFlow machine learn-  
 315 ing platform (Abadi et al., 2015). The detailed structures of those used networks are ex-  
 316 plained in Appendix A.

### 317 3.5 Loss functions and accuracy measurements

318 During training, we used five loss functions to optimize the network model: Mean  
 319 Squared Error (MSE), Mean Absolute Error (MAE), Huber loss, Mean Squared Loga-  
 320 rithmic Error (MSLE) and Logcosh loss. The mathematical formula for computing each  
 321 metric is shown in Table.1, where  $y_i$  represents the actual value of the  $i$ th sample, su-  
 322 perscript  $p$  means the predicted value, and  $n$  for the number of samples in each dataset.  
 323 MAE and MSE are the most common criteria for regression problems (Botchkarev, 2018).  
 324 The Huber loss function has a quadratic form for small values of errors, and a linear form  
 325 for large values of errors. The Huber loss can be considered as a combination of MAE  
 326 and MSE, which returns to MAE when the loss is large and MSE when the loss is small.  
 327 The  $\delta$  in the Huber function means a measure of the spread of the inliers, which is set  
 328 as 1.0 in our study. The disadvantage of the MSE is that it is sensitive to outliers be-  
 329 cause the larger the error, the more it overestimates the error. In contrast, MSLE, which  
 330 uses logarithmic error, does not overestimate even when the error is large because of its  
 331 logarithmic nature. The Logcosh loss is basically similar to MAE but gets closer to MSE  
 332 when losses are small. Though we used different loss functions for training, only the MAE  
 333 metric is used to assess the model accuracy because it is a common criterion for regres-  
 334 sion problems (Botchkarev, 2018).

Loss	Formula
MSE	$\frac{1}{n} \sum_{i=1}^n (y_i - y_i^p)^2$
MAE	$\frac{1}{n} \sum_{i=1}^n  y_i - y_i^p $
Huber	$\frac{1}{n} \sum_{i=1}^n \frac{1}{2} (y_i - y_i^p)^2, \text{ if }  y_i - y_i^p  \leq \delta$ $\frac{1}{n} \sum_{i=1}^n \delta \times ( y_i - y_i^p  - \frac{1}{2}\delta), \text{ if }  y_i - y_i^p  > \delta$
MSLE	$\frac{1}{n} \sum_{i=1}^n (\log(y_i + 1) - \log(y_i^p + 1))^2$
Logcosh	$\frac{1}{n} \sum_{i=1}^n \log \left( \frac{\exp(y_i^p - y_i) - \exp(y_i - y_i^p)}{2} \right)$

**Table 1.** Loss functions for the training process

### 3.6 Upscaling using Darcy flow solver for large scale sample

Since only the permeabilities of sub-volumes from the center core area were calculated by flow simulation, the remaining domain outside the center area was further divided into the same-size sub-volumes whose permeability can be predicted by the trained neural network. After the permeability map of the whole core is obtained, we can use the conventional Darcy flow solver to estimate the overall permeability of the whole core. In this study, we adopted the MATLAB Reservoir Simulation Toolbox (MRST) (Lie, 2019) to calculate the single-phase flow in the large core sample. The following governing equation for single-phase flow is solved by the two-point finite volume method in MRST:

$$\nabla \cdot \vec{v} = q, \quad \vec{v} = -\mathbf{K}\nabla P, \quad (3)$$

where,  $\vec{v}$  is the Darcy velocity,  $q$  is the flux and  $\mathbf{K}$  is the permeability tensor considering anisotropy. The sets of non-overlapped sub-volumes are directly used as the Cartesian grids in the Darcy flow solver. Fixed pressure boundary conditions are imposed on the inlet and outlet sides to generate a pressure gradient for driving the fluid. The no-flow conditions are applied on the rest of the boundaries. After the solver converged, the pressures for each grid and the flow flux across each face of the grid can be obtained. Finally, the upscaled permeability can be calculated from the flux of a single cross-section of the core sample.

## 4 Results and discussion

### 4.1 Permeability results of the direct flow simulation

The calculated permeability by the direct flow simulation is used as the training data for deep learning. Therefore, we first give detailed information about the permeability data for training. The histograms of the calculated permeability data for the sub-volumes (Fig. 5) indicate that the sample II has a much lower permeability compared with sample I. Most of the permeability values of sub-volumes in sample II are below 1.0 Darcy. The mean permeabilities are 10.8 Darcy and 5.03 Darcy for sample I and II, respectively. The standard deviation of permeability data for sample II is smaller than that for sample I, which means that the permeabilities are more concentrated in the low-value region for sample II. On the contrary, the permeabilities are widely distributed in sample I.

### 4.2 Evaluation of loss function

To examine which loss function gives the best performance in predicting permeability, we tested the five loss functions described in Section 3.5 using the basic Conv8 network. The accuracy for different loss functions is evaluated based on the MAE metric from test data of sample I.

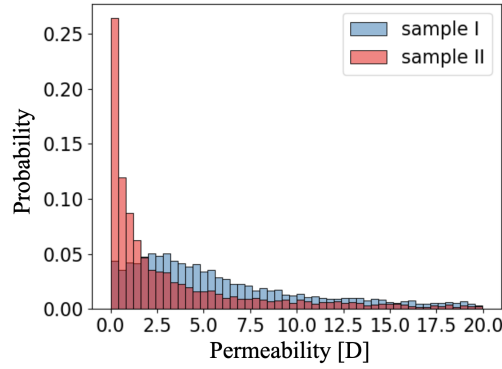


**Figure 5.** Histograms of the permeability for sample I and II.

Loss function	MSE	MAE	Huber	MSLE	Logcosh
Accuracy (MAE)	1.8957	1.9384	1.7639	2.8808	1.9488

**Table 2.** Accuracy of the five tested loss functions

369 The results (Table.2) show that the Huber loss function gives the best performance,  
 370 which is in agreement with the reference (N. Alqahtani et al., 2020). The Huber loss is  
 371 usually used for regression problems that are less sensitive to outliers (Huber, 1992). In  
 372 our training data, some of the sub-volumes with high porosities have extremely large per-  
 373 meabilities which may have a significant effect on the training accuracy. The Huber loss  
 374 function is able to suppress the effect of those high permeability data points. Therefore,  
 375 we decided to adopt the Huber loss function for the training process in all other networks  
 376 hereinafter.

### 377 4.3 Performance of different networks

378 The datasets of sample I are used for training the six neural networks described  
 379 in Section 3.4 to find out which network gives the best performance. The predicted val-  
 380 ues of permeabilities are plotted against the actual permeabilities obtained by direct nu-  
 381 merical simulation by different networks in Fig. 6 and 7 for Sample I. It can be seen that  
 382 the GoogLeNet and Resnet have better performance compared with the conventional Conv8  
 383 and VGG networks for the training data set. For the test data set, the Resnet gives the  
 384 best performance. Therefore, for sample II, only the results of Resnet are presented (Fig.8).  
 385 The accuracy in terms of the MAE for each network using the testing data set are shown  
 386 in Table.3 for both samples. With increasing the depth of the network, the accuracy is  
 387 improved. However, there are only limited gains in accuracy when just increasing the  
 388 layers of conventional networks (from VGG16 to VGG19). The reason is that the train-  
 389 ing process is performed by backpropagation method (Rumelhart et al., 1986), and it  
 390 becomes more difficult to correctly propagate the error when using more layers. Besides,  
 391 it is more easy to get stuck on a local optimum or saddle point during the training pro-  
 392 cess if we simply add more CNN layers. Increasing the number of layers may also lead  
 393 to overfitting. Resnet has a shortcut connection in the networks, which significantly im-  
 394 proves the performance when using a deep network. Our results also show that the Resnet  
 395 has the best performance with an MAE of 0.4546 and 0.2249 for samples I and II, re-  
 396 spectively. It should be noted that the sub-volume with high permeability has a large  
 397 contribution to the value of MAE. Because the sub-volumes with extremely high per-  
 398 meability are rare in the core, the learning accuracy is lower for these sub-volumes due

399 to the small number of their data sets (right-hand side figures in Fig. 7). The predic-  
 400 tion error from those sub-volumes may lead to a relatively high MAE value. Compared  
 401 to sample I, the permeabilities of sub-volumes in sample II are lower and more concen-  
 402 trated (Fig. 5), therefore the predicting accuracy for sample II is higher (Fig .8), and  
 403 the MAE for sample II is lower than that for sample I (Table 3).

Model	Layer number	MAE (sample I)	MAE (sample II)
Conv8	8	1.4226	0.8016
VGG16	16	1.2031	0.6939
VGG19	19	1.1348	0.9163
GoogLeNet-V1	22	1.1729	0.6141
GoogLeNet-V3	25	0.7589	0.4332
Resnet34	34	0.4546	0.2249

**Table 3.** The accuracy (MAE) of regression for various neural networks with different depths and structures

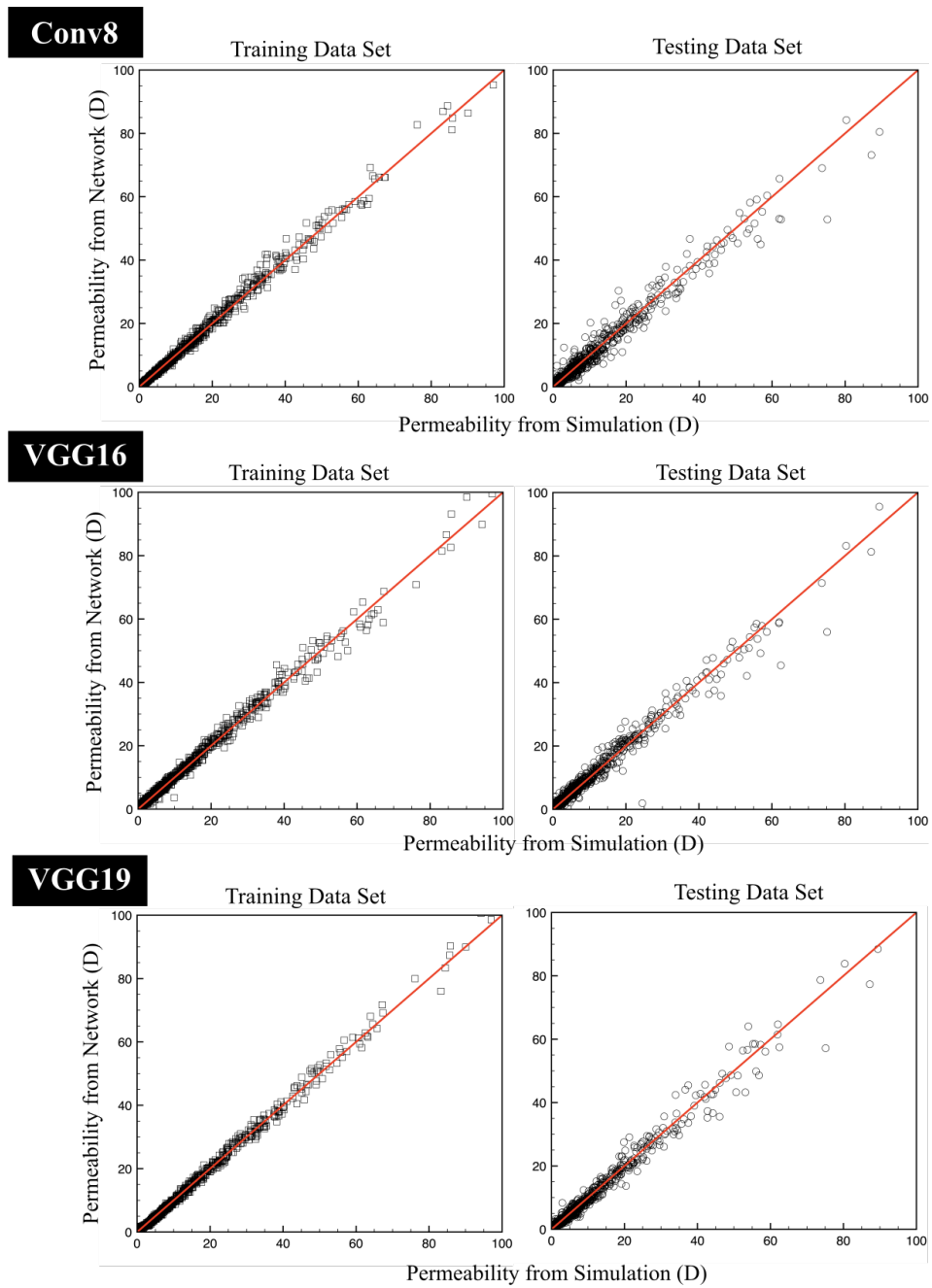
#### 404 4.4 Porosity prediction

405 In addition to the permeability, we also use the same approach to predict the porosi-  
 406 ties of the sub-volumes directly from the coarse scanned CT images. Here, we only use  
 407 the Resnet34 for the porosity prediction because it has the best performance for predict-  
 408 ing permeability. The corresponding training data for porosity was obtained from the  
 409 same segmented sub-volume models used in the LBM direct flow simulation.

410 The predicted results (Fig.9 and 10) show that the porosity can be accurately esti-  
 411 mated by the Resnet34 network. The MAEs of the test data with the trained networks  
 412 are 0.00193 and 0.00152 for samples I and II, respectively. The predictive accuracy for  
 413 porosity is much better compared with that for permeability. The reason is that the poros-  
 414 ity only depends on the gray scale histogram, while the permeability also depends on the  
 415 connectivity of pore spaces (e.g., the tortuosity of flow paths). Therefore, the porosity  
 416 is much easier to be characterized by using deep learning, which also implies that the  
 417 segmentation process can be tackled by the neural network (Wang, Shabaninejad, et al.,  
 418 2021). With the trained network for porosity, we are also able to obtain the porosity map  
 419 direct from the raw coarse CT images.

#### 420 4.5 Permeability map predicted by the trained network

421 Since the Resnet has the best performance in terms of permeability prediction, we  
 422 then estimated the permeabilities of the sub-volumes at the periphery of the rock core  
 423 (white boxes in the left image of Fig.2) by inputting the raw low-resolution images into  
 424 the trained Resnet network. The permeabilities of these unseen sub-volumes are predicted  
 425 using the best models' weights of Resnet. Because the training data of permeability was  
 426 obtained from the direct simulation of fluid flow along the axis direction of the core, we  
 427 rotated the CT images of the sub-volumes in order to consider the permeability anisotropy.  
 428 We then applied the trained networks to the rotated sub-volumes to estimate the per-  
 429 meability properties in the perpendicular directions (diagonal elements of the permeabil-  
 430 ity tensor). Note that the off-diagonal elements of permeability tensor are not consid-  
 431 ered in this study. The estimated permeability (core-axis direction) maps are illustrated  
 432 in (Fig.11), which indicate that the permeability of sample I is higher than that of sam-  
 433 ple II. These predicted permeability distributions using the neural network are qualita-  
 434 tively consistent with the ground truth data in Fig.5.



GoogLeNet-V1

**Figure 6.** Permeability values from simulation are plotted against the permeability using the network estimation (Conv8, VGG16 and VGG19). The red diagonal line represents  $y = x$ .

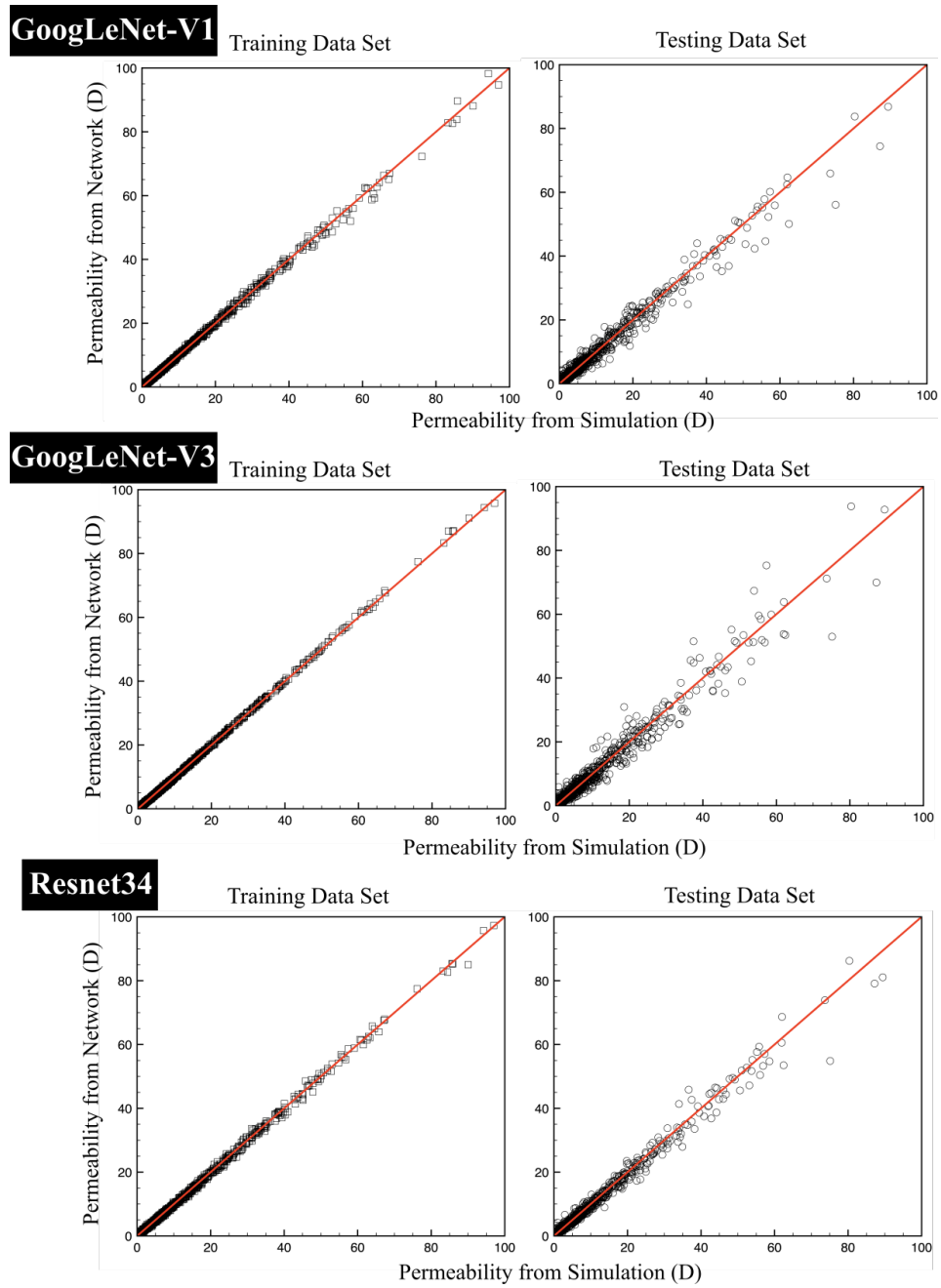


**Figure 7.** Permeability values from simulation are plotted against the permeability using the network estimation (GoogLeNet-V1, GoogLeNet-V3 and ResNet34). The red diagonal line represents  $y = x$ .

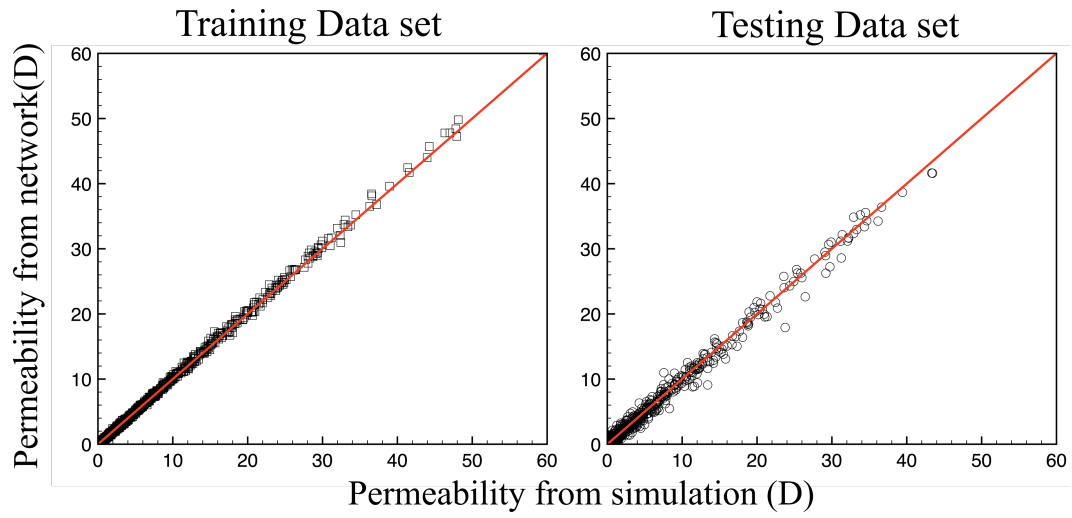


**Figure 8.** Permeability values from simulation are plotted against the permeability using the Resnet34 network estimation for sample II. The red diagonal line represents  $y = x$

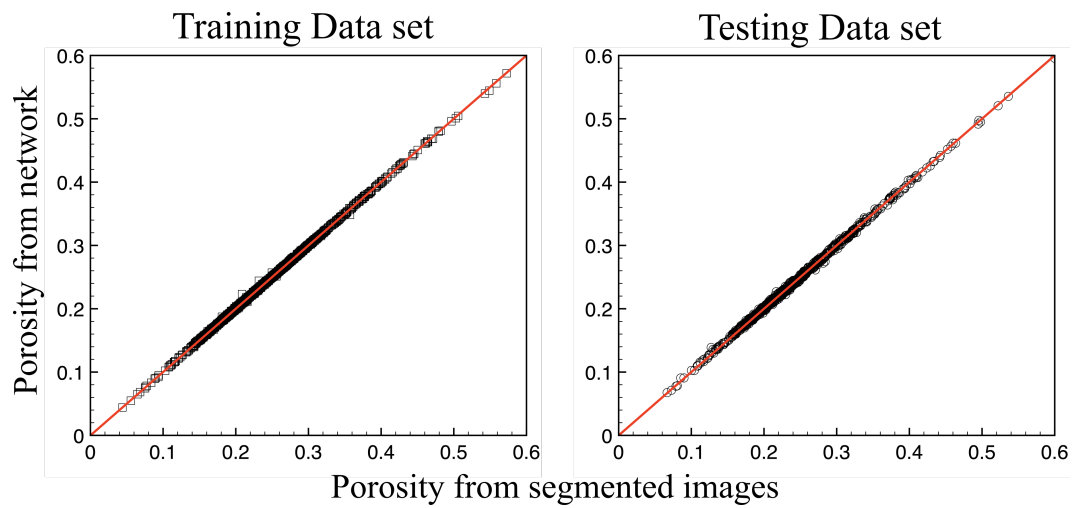


**Figure 9.** Porosity values from segmented rock images are plotted against the porosity using the Resnet34 network estimation for sample I. The red diagonal line represents  $y = x$ .

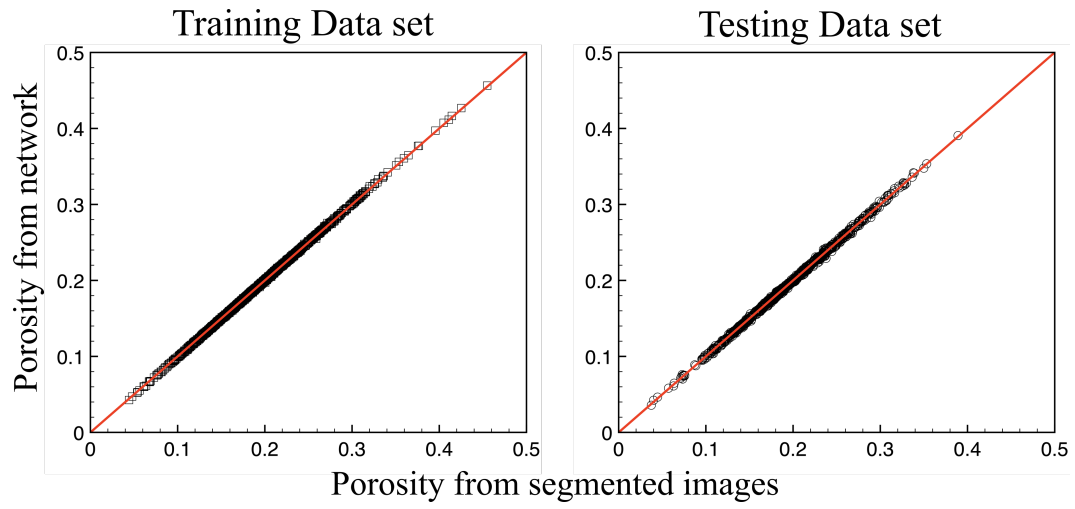


**Figure 10.** Porosity values from segmented rock images are plotted against the porosity using the Resnet34 network estimation for sample II. The red diagonal line represents  $y = x$ .

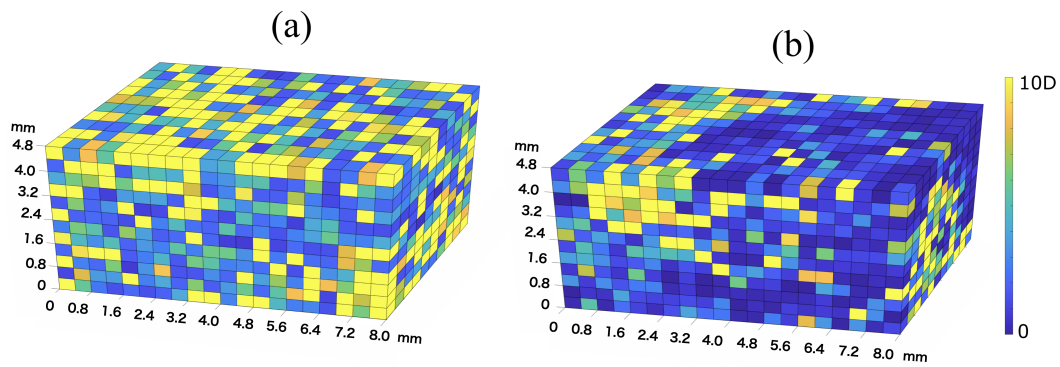


**Figure 11.** Permeability maps for the whole cores : (a) sample I; (b) sample II.

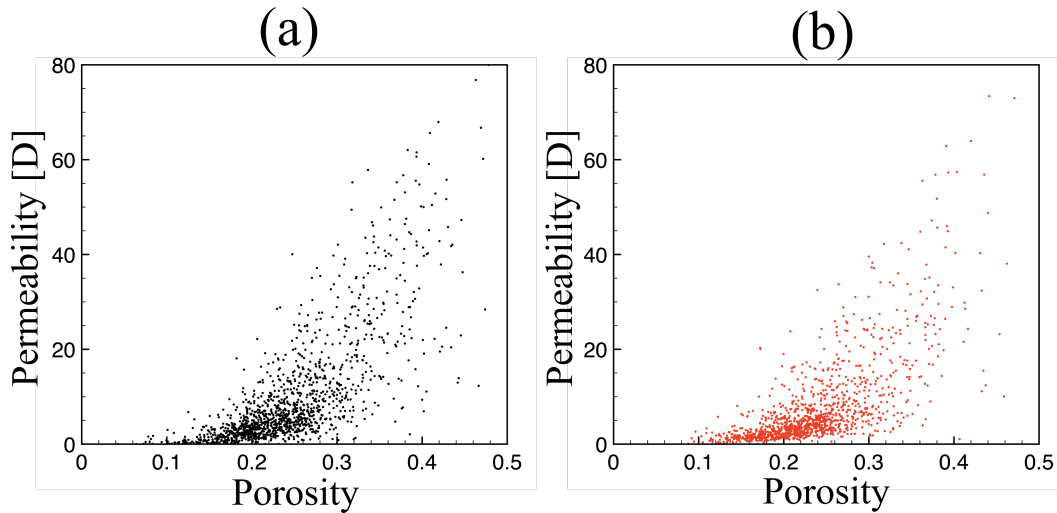


**Figure 12.** Relationship between the permeability and the porosity for sample I: (a) calculated ground truth data (b) predicted data.

435 The permeability values mainly depend on porosity. The simplest model describ-  
 436 ing the permeability-porosity relationship is the Kozeny-Carman (KC) model (CARMAN,  
 437 1937). As an evaluation of the capability of our approach, we also checked the permeability-  
 438 porosity relationship with respect to the predicted results. The plots of predicted porosity-  
 439 permeability scatters showed a similar pattern with the ground truth data for both sam-  
 440 ples (Fig.12 and 13). Therefore, our approach can also provide reliable data in terms of  
 441 the permeability-porosity relationship. Our data-driven approach for predicting perme-  
 442 ability and porosity is superior to the empirical KC models, which only related the perme-  
 443 ability to porosity neglecting the features of pore microstructures and the effect of flow  
 444 path connectivity. Besides, the empirical parameter in the KC model is usually not a constant  
 445 and is difficult to be determined (P. Xu & Yu, 2008). Unlike this conventional empirical  
 446 model, our CNN-based approach is able to predict the permeability variation considering  
 447 the effect of microstructures by preserving the information of the original CT  
 448 images.

449 This permeability mapping in low-resolution 3D images by using the neural network  
 450 lays the groundwork for the following permeability upscaling and the computation  
 451 of effective permeability at the large core scale.

#### 452 4.6 Upscaled permeability of the whole core

453 The permeability map is then plugged into the Darcy flow solver (Lie, 2019) to calculate  
 454 the pressure distribution and flux in the whole sample using the boundary conditions  
 455 described in Section 3.6. A rectangular cuboid computational domain for the Darcy  
 456 flow solver is extracted from the core samples with a grids size of  $10 \times 12 \times 20$ . Each grid  
 457 was assigned the predicted permeabilities in three directions. The gravity was not considered  
 458 in the Darcy flow simulation. The implementation of this Darcy flow simulation can be found  
 459 in the reference documentation (*MRST Flow Solver Tutorial*, n.d.). Finally, the solution for  
 460 flow and pressure in the entire core can be obtained by solving the constructed linear  
 461 system using two-point flux schemes (Lie, 2019). The results of pressure distribution  
 462 indicated that the pressure gradient along the flow direction in sample I is relatively  
 463 uniform (Fig.14) because the permeability map is more homogeneous compared with  
 464 sample II (Fig. 11). On the contrary, sample II has a relatively heterogeneous per-

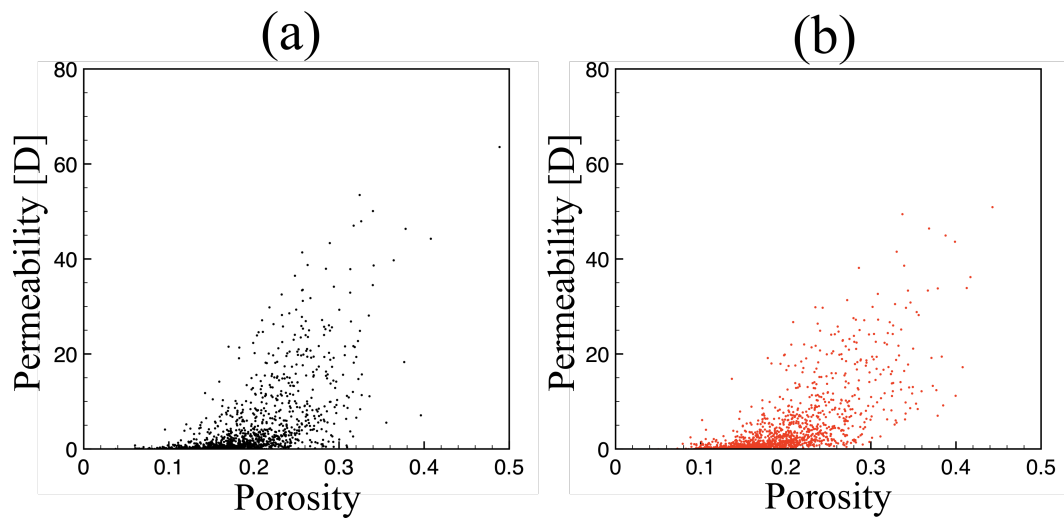


**Figure 13.** Relationship between the permeability and the porosity for sample II: (a) calculated ground truth data (b) predicted data.

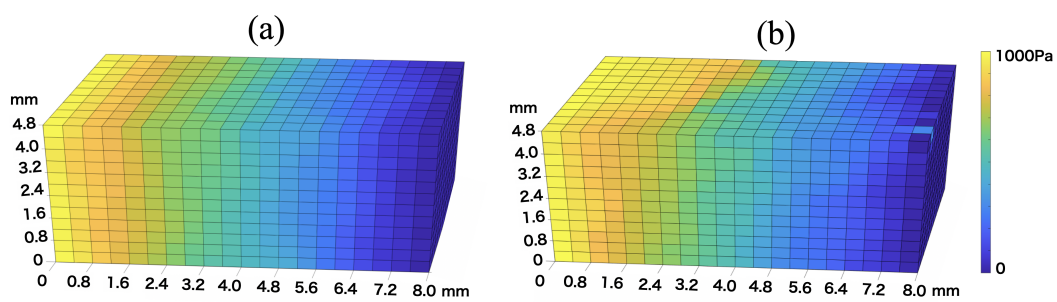


**Figure 14.** Pressure distributions of the whole core obtained from the Darcy flow solver: (a) sample I (b) sample II.

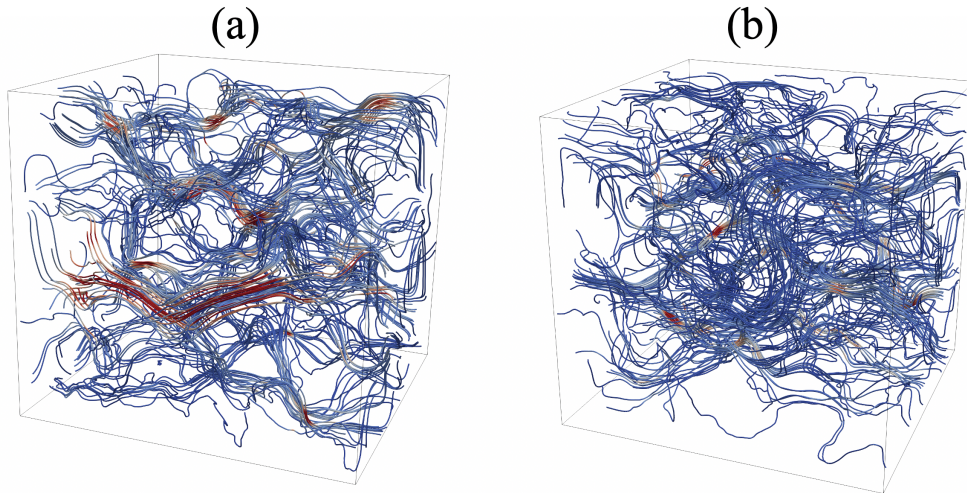


**Figure 15.** Velocity stream lines of the two center cores obtained from the direct LBM flow simulation: (a) sample I (b) sample II; red and blue colors indicate the high and low velocity sites, respectively .

465 permeability distribution resulting in a non-uniform pressure drop along the flow direction  
 466 (Fig.14).

467 Then the upscaled permeability can be calculated from the flux distribution inside  
 468 the computation domain by the Darcy flow solver. To evaluate the accuracy of the up-  
 469 scaled permeability, we also calculated the permeability at the center region of the same  
 470 core sample for comparison using the direct LBM flow simulation because only high-resolution  
 471 micro-CT images of the center area are available. Though, the low-resolution images ( $8\mu m$ )  
 472 of the whole core can somehow be segmented for flow simulation to obtain the perme-  
 473 ability of the whole area. However, the uncertainty of the segmentation due to the low  
 474 resolution may lead to a large error in the direct flow simulation. Besides, the domain  
 475 size of the whole core is too large for LBM simulation, which is beyond the limitation  
 476 of our computational resources. Therefore, the permeability of only the center core area  
 477 is fully calculated by LBM simulation as the ground truth reference value. For the Boise  
 478 sandstone, the simulation domain of  $690 \times 690 \times 690$  ( $1.38mm$  cube) used in the LBM cal-  
 479 culation is large enough to reach the REV size. The calculated flow velocity streamlines  
 480 (Fig. 15) indicated that sample I has highly connected flow paths, which leads to high  
 481 velocity sites in large pore spaces. On the other hand, the flow velocities in sample II  
 482 are lower due to the highly tortuous flow paths (Fig. 15). As a result, the permeabil-  
 483 ity of sample II is lower than that of sample I.

484 We also use pore-network modeling (PNM) to calculate the permeability for the  
 485 center and the whole core areas with two different resolutions, respectively. PNM is an  
 486 indirect method that solves simplified transport equations on idealized pore geometries  
 487 to estimate flow properties (Blunt, 2001). Because the pore geometries in PNM are rep-  
 488 resented by simple spheres and pipes, the accurate shape of boundaries between pore spaces  
 489 and solid grain is not necessary. Since the pore structure can still be identified to some  
 490 extent from the low-resolution images, therefore the PNM can be applied to the whole  
 491 core area. Here, the pore network rock model is reconstructed by using the skeleton ex-  
 492 traction combined with a watershed algorithm (Youssef et al., 2007). The large-scale per-  
 493 meabilities obtained by PNM, LBM, and CNN are summarized in Table. 4.

Sample	I	II
K of center core (PNM; high resolution)	5.15D	0.75D
K of whole core (PNM; low resolution)	12.8D	3.53D
K of center core (LBM; high resolution)	4.83D	1.89D
K of whole core (CNN; low resolution)	5.85D	1.53D

**Table 4.** Large scale permeabilities K obtained by different methods

494 The upscaled permeabilities based on CNN agreed well with the data obtained by  
495 the LBM, which have relative error of 21% and 19% for samples I and II, respectively.  
496 The PNM can roughly estimate the permeability of the center core with high-resolution  
497 images but failed to predict the permeability when using low-resolution data. For sam-  
498 ple II, the PNM underestimates the permeability even using the high-resolution images.  
499 Because sample II has low porosity which means that the size of pore bodies is small,  
500 it becomes inaccurate to represent the pore spaces by simple spheres and pipes in PNM.  
501 In addition, PNM is highly sensitive to image resolution. In low-resolution images, the  
502 pore throats are depicted by intermediate grayscale voxels which may be closed during  
503 the segmentation process. Such uncertainties in the segmentation process for low-resolution  
504 images leads to large errors in PNM predictions. On the other hand, our upscaling method  
505 direct utilized the raw low-resolution images without the segmentation process, and there-  
506 fore preserves the grayscale information related to pore, results in higher accuracy in pre-  
507 dicting the permeability. The measured permeability of the Boise sandstone by the ex-  
508 periment performed on a meter scale is 2.8D, which is between the predicted values of  
509 the two samples. This is reasonable because samples I and II are extracted from the high  
510 and low porosity areas, respectively. Therefore, we can conclude that our CNN-based  
511 upscaling method is able to estimate the reliable value of permeability at a large scale.

512 Since both samples I and II are extracted from the same Boise sandstone core at  
513 different locations, the general features of the pore structures of these two samples may  
514 have similarities. Therefore, we also tested the prediction performance for the perme-  
515 ability map of sample II using the neural network trained by the data extracted from  
516 sample I (i.e., using the best network weights obtained from the training process of sam-  
517 ple I). The predicted permeability map of sample II (Fig.16) presented a very similar dis-  
518 tribution to the native permeability map (Fig.11(b)), namely, the predicted permeabil-  
519 ity map using the CT images and the neural network trained by the data from the same  
520 sample. The upscaled permeability of sample II from the permeability map predicted  
521 by the sample I's network is 2.47D, which is slightly overestimated compared with the  
522 ground-truth value (1.53D) because most of the training data in sample I has higher poros-  
523 ity and permeability than sample II. Nevertheless, the accuracy is still much better than  
524 that obtained by PNM. The upscaled permeability predicted by the combination of sam-  
525 ple II's geometry (CT images) and sample I's neural network is very close to the exper-  
526 imental data (2.8D).

527 From the above investigation, we can conclude that the trained neural network is  
528 applicable for the unseen sample of the same rock type (Boise sandstone used here). How-  
529 ever, it must be mentioned that, for the other rock types, we need to carry out the same  
530 deep learning process again to establish a specialized well-trained neural network because  
531 different rock types usually have different characteristics of pore geometry (e.g., pore con-  
532 nectivities and porosities) which leads to different weights of the neuron. Finally, we could  
533 build a trained neuron network database for each type of rock, which enables us to quickly  
534 estimate the permeability directly from the raw CT images without carrying out the costly  
535 and time-consuming experiment.

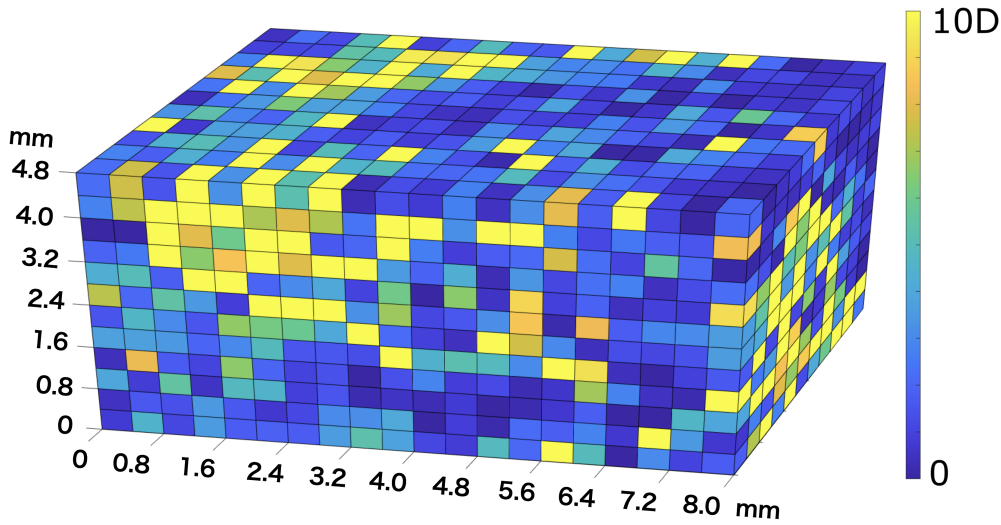


**Figure 16.** Permeability map of the sample II predicted by the neural network trained using data extracted from sample I.

## 536 5 Summary

537 This study presented a workflow to predict the upscaled absolute permeability of  
 538 the large rock core directly from CT images whose resolution is insufficient to allow di-  
 539 rect permeability computation. Our approach used a deep learning technique to estab-  
 540 lish correlations between low-resolution image characteristics and high-resolution com-  
 541 puted permeability by overlapping registered CT images. The training data sets for deep  
 542 learning consist of pairs of coarse scanned raw CT images and their corresponding per-  
 543 meability value obtained by performing LBM simulation on high-resolution CT images.  
 544 During this process, image registration is vital for integrating micro-CT images acquired  
 545 at two different resolutions. Six different neural networks were trained to check the per-  
 546 formance for predicting the permeability of the low-resolution images. The Resnet showed  
 547 the best performance and can accurately predict the spatial variations of both porosity  
 548 and permeability properties. The permeability map of large field of view can be directly  
 549 obtained from the raw low-resolution CT images by the neural networks without the seg-  
 550 mentation process. Based on the permeability map, the upscaled permeability of the en-  
 551 tire core can be calculated by the Darcy flow solver. The upscaled permeability showed  
 552 a good agreement with the experiment data, which indicates that our deep-learning-based  
 553 upscaling method allows estimating the large-scale permeability of core samples while  
 554 preserving the effects of fine-scale variations due to local heterogeneity.

## 555 6 Acknowledgement

556 We gratefully acknowledge funding from Japan Oil, Gas and Metals National Cor-  
 557 poration (JOGMEC). This study was also supported by the Japan Society for the Pro-  
 558 motion of Science (JSPS) through a Grant-in-Aid for Challenging Exploratory Research  
 559 (Grant No. JP20K20948) and a Grant-in-Aid for Scientific Research (Grant No. JP22K03927).

## 560 7 Data Availability Statement

561 The datasets and code used in this study are available from Mendeley repository  
 562 <http://dx.doi.org/10.17632/7jmfpszpws7.1>

## 563 Appendix A Neural network architectures

564 The architectures of neural network using in this study are presented here. In the  
 565 following figures, relu refers to the rectified linear unit activation (Nair & Hinton, 2010).  
 566 The blocks with five numbers inside indicate the convolution layer, in which the first three  
 567 numbers refer to the kernel size in three dimensions, the second number means stride  
 568 size, and the last shows the filter number. MP means the max pooling layer with ker-  
 569 nel size shown in the block. BN refers to batch normalization (Ioffe & Szegedy, 2015),  
 570 GP means the global average pooling layer, FC means filter concatenation, and DP in  
 571 the dense block refers to the dropout layer applied after the dense layer. The dense layer  
 572 size is shown at the top of the dense block.

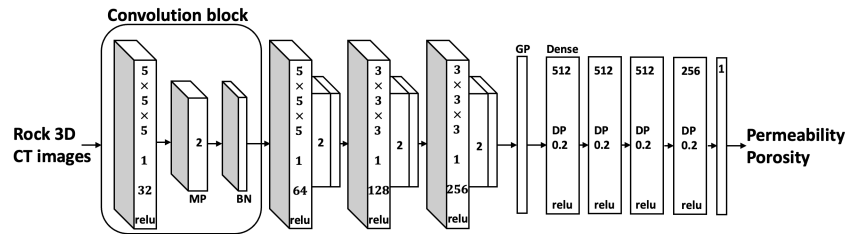


Figure A1. Conv8 network architecture.

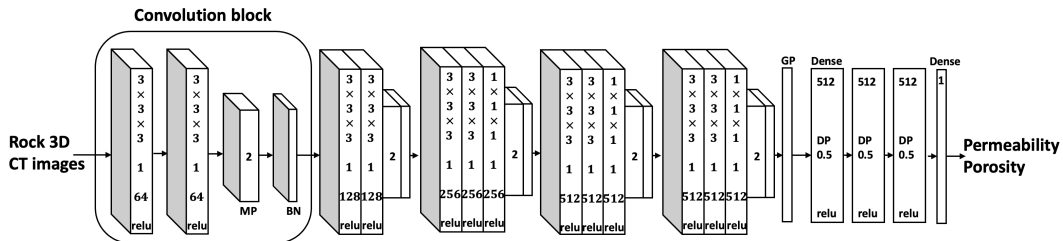


Figure A2. VGG16 network architecture

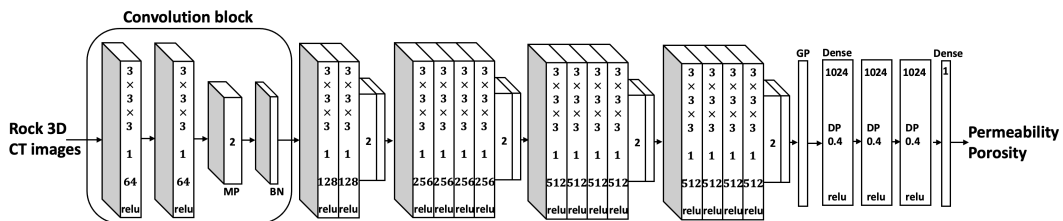


Figure A3. VGG19 network architecture

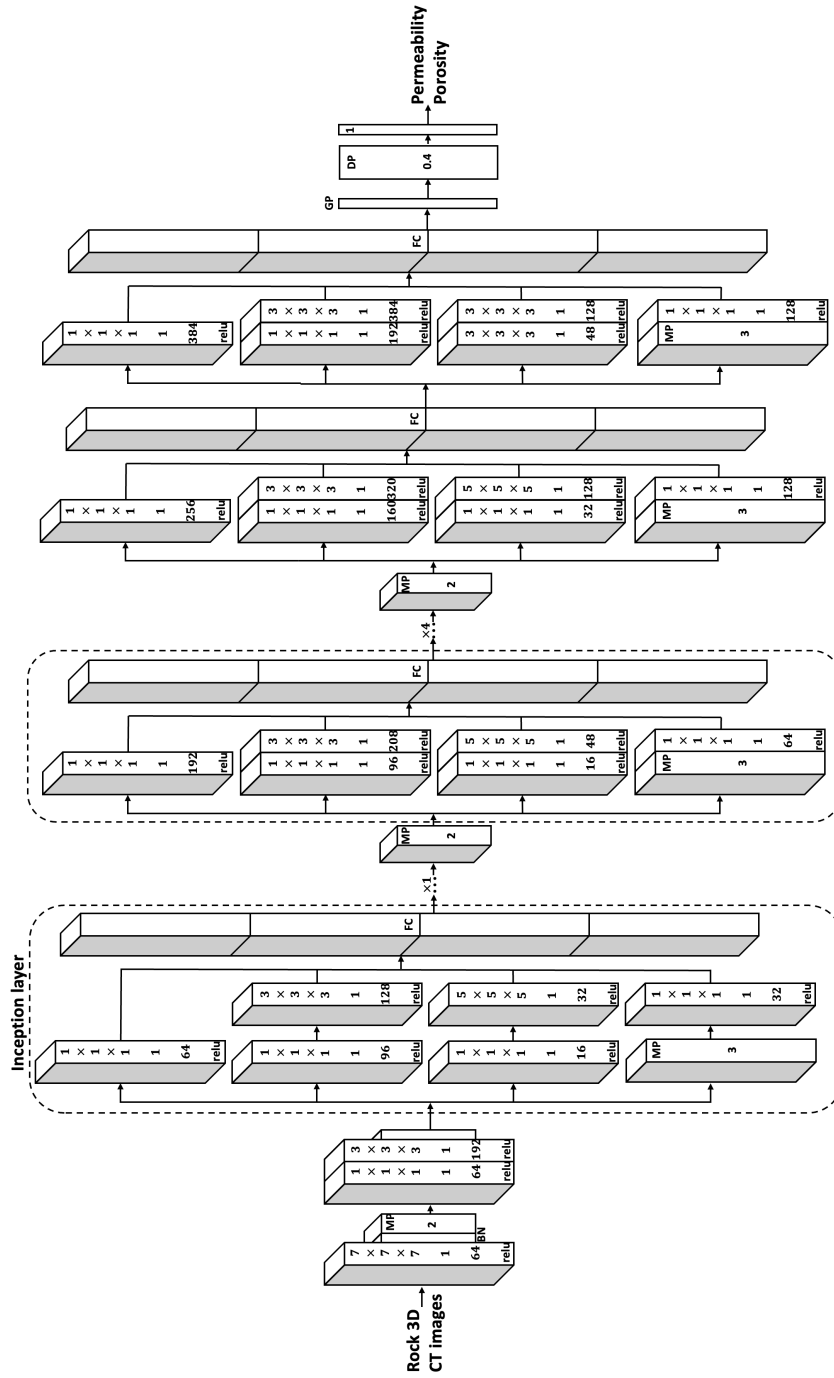


Figure A4. GoogLeNet-V1 network architecture

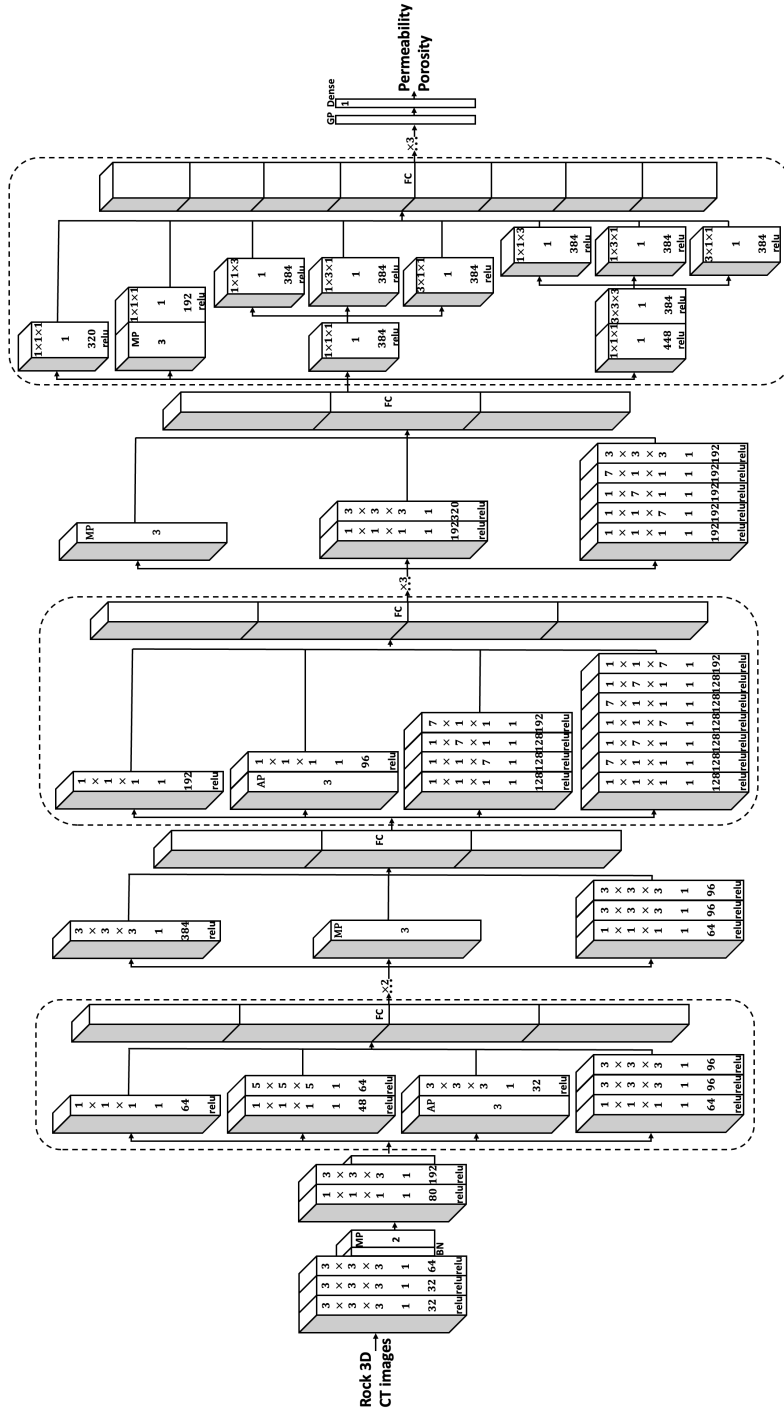


Figure A5. GoogLeNet-V3 network architecture

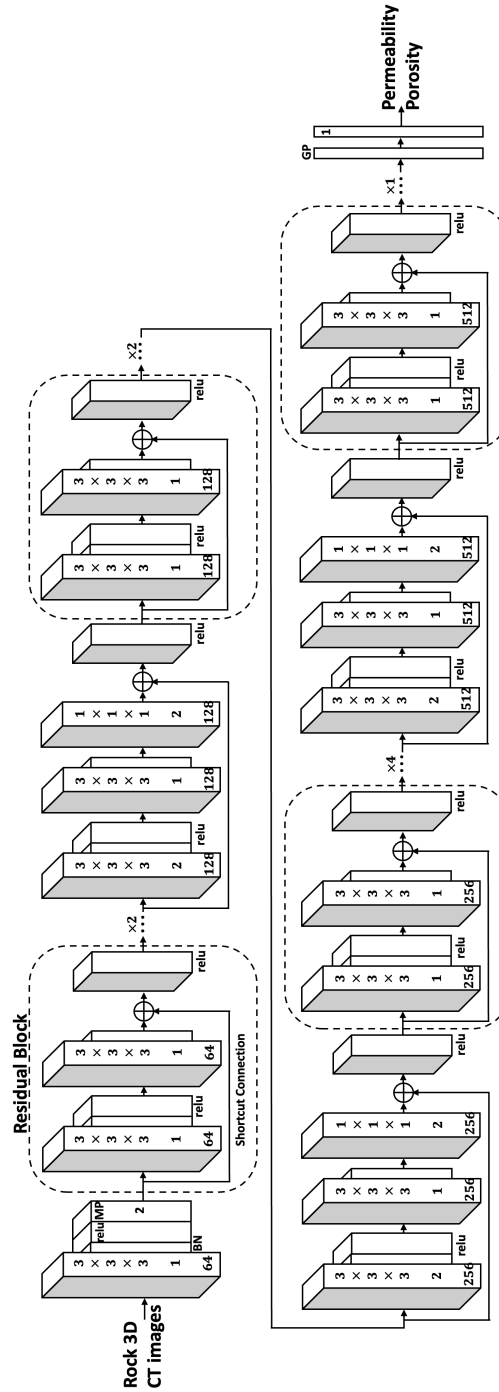


Figure A6. Resnet34 network architecture

573 **References**

574 Abadi, M., Agarwal, A., Barham, P., Brevdo, E., Chen, Z., Citro, C., ... Zheng,  
 575 X. (2015). *TensorFlow: Large-scale machine learning on heterogeneous sys-*  
 576 *tems*. Retrieved from <http://tensorflow.org/> (Software available from  
 577 tensorflow.org)  
 578 Alqahtani, N., Alzubaidi, F., Armstrong, R. T., Swietojanski, P., & Mostaghimi, P.

- (2020). Machine learning for predicting properties of porous media from 2d x-ray images. *Journal of Petroleum Science and Engineering*, *184*, 106514.
- Alqahtani, N. J., Chung, T., Wang, Y. D., Armstrong, R. T., Swietojski, P., & Mostaghimi, P. (2021). Flow-based characterization of digital rock images using deep learning. *SPE Journal*, *26*(04), 1800–1811.
- Arns, C. H., Knackstedt, M. A., Pinczewski, M. V., & Lindquist, W. (2001). Accurate estimation of transport properties from microtomographic images. *Geophysical research letters*, *28*(17), 3361–3364.
- Bizhani, M., Ardakani, O. H., & Little, E. (2022). Reconstructing high fidelity digital rock images using deep convolutional neural networks. *Scientific reports*, *12*(1), 1–14.
- Blunt, M. J. (2001). Flow in porous media—pore-network models and multiphase flow. *Current opinion in colloid & interface science*, *6*(3), 197–207.
- Blunt, M. J., Bijeljic, B., Dong, H., Gharbi, O., Iglauer, S., Mostaghimi, P., ... Pentland, C. (2013). Pore-scale imaging and modelling. *Advances in Water resources*, *51*, 197–216.
- Boek, E. S., & Venturoli, M. (2010). Lattice-boltzmann studies of fluid flow in porous media with realistic rock geometries. *Computers & Mathematics with Applications*, *59*(7), 2305–2314.
- Botchkarev, A. (2018). Performance metrics (error measures) in machine learning regression, forecasting and prognostics: Properties and typology. *arXiv preprint arXiv:1809.03006*.
- Botha, P. W., & Sheppard, A. P. (2016). Mapping permeability in low-resolution micro-ct images: A multiscale statistical approach. *Water Resources Research*, *52*(6), 4377–4398.
- CARMAN, P. C. (1937). Fluid flow through granular beds. *Trans. Inst. Chem. Eng.*, *15*, 150-166. Retrieved from <https://ci.nii.ac.jp/naid/10003392892/>
- Da Wang, Y., Armstrong, R. T., & Mostaghimi, P. (2019). Enhancing resolution of digital rock images with super resolution convolutional neural networks. *Journal of Petroleum Science and Engineering*, *182*, 106261.
- Dehghan Khalili, A., Arns, J.-Y., Hussain, F., Cinar, Y., Pinczewski, W., Arns, C. H., et al. (2013). Permeability upscaling for carbonates from the pore scale by use of multiscale x-ray-ct images. *SPE Reservoir Evaluation & Engineering*, *16*(04), 353–368.
- d’Humières, D. (1992). Generalized lattice-boltzmann equations. *Rarefied gas dynamics*.
- Fredrich, J., Greaves, K., & Martin, J. (1993). Pore geometry and transport properties of fontainebleau sandstone. In *International journal of rock mechanics and mining sciences & geomechanics abstracts* (Vol. 30, pp. 691–697).
- Goral, J., Walton, I., Andrew, M., & Deo, M. (2019). Pore system characterization of organic-rich shales using nanoscale-resolution 3d imaging. *Fuel*, *258*, 116049.
- Guo, Z., & Shu, C. (2013). *Lattice boltzmann method and its application in engineering* (Vol. 3). World Scientific.
- He, K., Zhang, X., Ren, S., & Sun, J. (2016). Deep residual learning for image recognition. In *Proceedings of the ieee conference on computer vision and pattern recognition* (pp. 770–778).
- Hong, J., & Liu, J. (2020, August). Rapid estimation of permeability from digital rock using 3D convolutional neural network. *Computational Geosciences*, *24*(4), 1523–1539. doi: 10.1007/s10596-020-09941-w
- Huber, P. J. (1992). Robust estimation of a location parameter. In *Breakthroughs in statistics* (pp. 492–518). Springer.
- Ioffe, S., & Szegedy, C. (2015). Batch normalization: Accelerating deep network training by reducing internal covariate shift. In *International conference on*

- 634 *machine learning* (pp. 448–456).
- 635 Jiang, F., Liu, H., Chen, X., & Tsuji, T. (2022). A coupled lbm-dem method for  
636 simulating the multiphase fluid-solid interaction problem. *Journal of Computa-*  
637 *tional Physics*, 110963.
- 638 Jiang, F., Matsumura, K., Ohgi, J., & Chen, X. (2021). A gpu-accelerated fluid-  
639 structure-interaction solver developed by coupling finite element and lattice  
640 boltzmann methods. *Computer Physics Communications*, 259, 107661.
- 641 Jiang, F., & Tsuji, T. (2014). Changes in pore geometry and relative permeability  
642 caused by carbonate precipitation in porous media. *Physical Review E*, 90(5),  
643 053306.
- 644 Jiang, F., & Tsuji, T. (2015). Impact of interfacial tension on residual co2 clusters in  
645 porous sandstone. *Water Resources Research*, 51(3), 1710–1722.
- 646 Jiang, F., & Tsuji, T. (2017). Estimation of three-phase relative permeability by  
647 simulating fluid dynamics directly on rock-microstructure images. *Water Re-*  
648 *sources Research*, 53(1), 11–32.
- 649 Juanes, R., Spiteri, E., Orr Jr, F., & Blunt, M. (2006). Impact of relative permeabil-  
650 ity hysteresis on geological co2 storage. *Water resources research*, 42(12).
- 651 Lake, L. W., Johns, R., Rossen, B., Pope, G. A., et al. (2014). *Fundamentals of en-*  
652 *hanced oil recovery* (Vol. 1). Society of Petroleum Engineers Richardson, TX.
- 653 LeCun, Y., Bottou, L., Bengio, Y., & Haffner, P. (1998). Gradient-based learning  
654 applied to document recognition. *Proceedings of the IEEE*, 86(11), 2278–2324.
- 655 Li, S., Jiang, F., Wei, B., Hou, J., & Liu, H. (2021). Prediction of three-phase rela-  
656 tive permeabilities of berea sandstone using lattice boltzmann method. *Physics*  
657 *of Fluids*, 33(6), 063302.
- 658 Lie, K.-A. (2019). Single-phase flow. In *An introduction to reservoir simulation us-*  
659 *ing matlab/gnu octave: User guide for the matlab reservoir simulation toolbox*  
660 *(mrst)* (p. 111–112). Cambridge University Press.
- 661 Liu, H., Lu, Y., Li, S., Yu, Y., & Sahu, K. C. (2021). Deformation and breakup of  
662 a compound droplet in three-dimensional oscillatory shear flow. *International*  
663 *Journal of Multiphase Flow*, 134, 103472.
- 664 Menke, H. P., Maes, J., & Geiger, S. (2021, December). Upscaling the poros-  
665 ity–permeability relationship of a microporous carbonate for Darcy-scale  
666 flow with machine learning. *Scientific Reports*, 11(1), 2625. doi: 10.1038/  
667 s41598-021-82029-2
- 668 *MRST Flow Solver Tutorial*. (n.d.). [https://www.sintef.no/projectweb/mrst/](https://www.sintef.no/projectweb/mrst/documentation/tutorials/flow-solver-tutorial/)  
669 [documentation/tutorials/flow-solver-tutorial/](https://www.sintef.no/projectweb/mrst/documentation/tutorials/flow-solver-tutorial/).
- 670 Nair, V., & Hinton, G. E. (2010). Rectified linear units improve restricted boltz-  
671 mann machines. In *Icml*.
- 672 Pan, C., Luo, L.-S., & Miller, C. T. (2006). An evaluation of lattice boltzmann  
673 schemes for porous medium flow simulation. *Computers & fluids*, 35(8-9), 898–  
674 909.
- 675 Pape, H., Clauser, C., & Iffland, J. (1999). Permeability prediction based on fractal  
676 pore-space geometry. *Geophysics*, 64(5), 1447–1460.
- 677 Rabbani, A., & Babaei, M. (2019). Hybrid pore-network and lattice-boltzmann  
678 permeability modelling accelerated by machine learning. *Advances in water re-*  
679 *sources*, 126, 116–128.
- 680 Raeini, A. Q., Blunt, M. J., & Bijeljic, B. (2012). Modelling two-phase flow in  
681 porous media at the pore scale using the volume-of-fluid method. *Journal of*  
682 *Computational Physics*, 231(17), 5653–5668.
- 683 Rumelhart, D. E., Hinton, G. E., & Williams, R. J. (1986). Learning representations  
684 by back-propagating errors. *nature*, 323(6088), 533–536.
- 685 Santos, J. E., Xu, D., Jo, H., Landry, C. J., Prodanović, M., & Pyrcz, M. J. (2020,  
686 April). PoreFlow-Net: A 3D convolutional neural network to predict fluid flow  
687 through porous media. *Advances in Water Resources*, 138, 103539. doi: 10  
688 .1016/j.advwatres.2020.103539

- 689 Shah, S., Gray, F., Crawshaw, J., & Boek, E. (2016). Micro-computed tomography  
690 pore-scale study of flow in porous media: Effect of voxel resolution. *Advances*  
691 *in water resources*, *95*, 276–287.
- 692 Shan, X., Yuan, X.-F., & Chen, H. (2006). Kinetic theory representation of hydrody-  
693 namics: a way beyond the navier–stokes equation. *Journal of Fluid Mechanics*,  
694 *550*, 413–441.
- 695 Simonyan, K., & Zisserman, A. (2014). Very deep convolutional networks for large-  
696 scale image recognition. *arXiv preprint arXiv:1409.1556*.
- 697 Suzuki, A., Fukui, K.-i., Onodera, S., Ishizaki, J., & Hashida, T. (2022). Data-  
698 driven geothermal reservoir modeling: Estimating permeability distributions by  
699 machine learning. *Geosciences*, *12*(3), 130.
- 700 Szegedy, C., Liu, W., Jia, Y., Sermanet, P., Reed, S., Anguelov, D., . . . Rabinovich,  
701 A. (2015). Going deeper with convolutions. In *Proceedings of the ieee confer-*  
702 *ence on computer vision and pattern recognition* (pp. 1–9).
- 703 Tester, J. W., Anderson, B. J., Batchelor, A., Blackwell, D., DiPippo, R., Drake, E.,  
704 . . . others (2006). The future of geothermal energy. *Massachusetts Institute of*  
705 *Technology*, 358.
- 706 Wang, Y. D., Blunt, M. J., Armstrong, R. T., & Mostaghimi, P. (2021, April). Deep  
707 learning in pore scale imaging and modeling. *Earth-Science Reviews*, *215*,  
708 103555. doi: 10.1016/j.earscirev.2021.103555
- 709 Wang, Y. D., Shabaninejad, M., Armstrong, R. T., & Mostaghimi, P. (2021). Deep  
710 neural networks for improving physical accuracy of 2d and 3d multi-mineral  
711 segmentation of rock micro-ct images. *Applied Soft Computing*, *104*, 107185.  
712 Retrieved from [https://www.sciencedirect.com/science/article/pii/](https://www.sciencedirect.com/science/article/pii/S1568494621001083)  
713 [S1568494621001083](https://www.sciencedirect.com/science/article/pii/S1568494621001083) doi: <https://doi.org/10.1016/j.asoc.2021.107185>
- 714 Worthington, P. F. (2004). The effect of scale on the petrophysical estimation of  
715 intergranular permeability. *Petrophysics-The SPWLA Journal of Formation*  
716 *Evaluation and Reservoir Description*, *45*(01), 59–72.
- 717 Xu, P., & Yu, B. (2008). Developing a new form of permeability and kozeny–carman  
718 constant for homogeneous porous media by means of fractal geometry. *Ad-*  
719 *vances in water resources*, *31*(1), 74–81.
- 720 Xu, Z.-J. (2012). Homogenization and upscaling for diffusion, heat conduction, and  
721 wave propagation in heterogeneous materials. *Communications in Theoretical*  
722 *Physics*, *57*(3), 348.
- 723 Yang, J., & Boek, E. S. (2013). A comparison study of multi-component lattice  
724 boltzmann models for flow in porous media applications. *Computers & Mathe-*  
725 *matics with Applications*, *65*(6), 882–890.
- 726 Yang, L., Yang, J., Boek, E., Sakai, M., & Pain, C. (2019). Image-based simulations  
727 of absolute permeability with massively parallel pseudo-compressible stabilised  
728 finite element solver. *Computational Geosciences*, *23*(5), 881–893.
- 729 You, N., Li, Y. E., & Cheng, A. (2021). 3d carbonate digital rock reconstruction  
730 using progressive growing gan. *Journal of Geophysical Research: Solid Earth*,  
731 *126*(5), e2021JB021687.
- 732 Youssef, S., Rosenberg, E., Gland, N. F., Kenter, J. A., Skalinski, M., & Vizika,  
733 O. (2007). High resolution ct and pore-network models to assess petrophys-  
734 ical properties of homogeneous and heterogeneous carbonates. In *Spe/eage*  
735 *reservoir characterization and simulation conference*.
- 736 Zhai, H., Xue, Z., Park, H., Aizawa, Y., Baba, Y., & Zhang, Y. (2020). Migration  
737 characteristics of supercritical co2 microbubble flow in the berea sandstone  
738 revealed by voxel-based x-ray computed tomography imaging analysis. *Journal*  
739 *of Natural Gas Science and Engineering*, *77*, 103233.
- 740 Zhang, Y., Jiang, F., & Tsuji, T. (2022). Influence of pore space heterogeneity  
741 on mineral dissolution and permeability evolution investigated using lattice  
742 boltzmann method. *Chemical Engineering Science*, *247*, 117048.